scientific reports



OPEN

Exploiting hafnium nitride nanostructures for polarization-insensitive and wideband infrared absorption

Khaled Aliqab¹, Meshari Alsharari^{1⊠}, Spyridon Nektarios Daskalakis² & Ammar Armghan¹

Investigating new plasmonic materials for the design of nanostructured absorbers is in high demand. This study explores the possibility of using transition metal nitride, HfN, in the implementation of an infrared nanostructured absorber. To design and analyze a broadband absorber, a simple and easily fabricable HfN-based circular ring is mounted over a dielectric substrate with a metal backing. The designed HfN-based metasurface absorber manifests a good absorption characteristic, maintaining an absorption rate above 90% over the wide operational wavelength range of 700 nm to 1700 nm. When the incident angles of the optical light are changed from normal to higher values, the absorption characteristics of the metasurface absorber remain stable and even at θ = 60°, it shows a reasonable absorption rate of over 70%. Furthermore, it also performs insensitive behavior to the varying polarization angles owing to its inherent four-fold symmetry. Additionally, the multi-reflection cavity model has been used to validate the simulation results of the metasurface absorber. Its broad absorption bandwidth, mechanical stability, and thermal robustness make it a promising material for thermophotovoltaics and solar cells applications.

Keywords Metamaterial, Hafnium nitride, Absorber, Nanostructured, Solar cell, Wideband

A significant reputation has been recognized for metamaterials due to their incorporation into optical and microwave systems and their wide range of applications in various communication technologies, security, imaging, biomedicine, and sensing¹⁻⁸. They are metal-or dielectric-based artificial micro/nano resonators, designed to achieve unusual and exotic light-manipulation properties which are not possible with natural materials⁹⁻¹¹. Numerous applications for filters, lenses, antennas, sensors, converters, and other optical and microwave devices are implemented by these man-made structures, which come in a variety of sizes, shapes, and configurations^{4,6,12-21}.

Nanoscale optical light manipulation allows for the development of a wide range of optical phenomena, such as meta-lensing, plasmon induced transparency, perfect absorption and optical sensing^{22–28}. The need for nanostructured absorbers has been rising because of their utilization in many interesting applications, including solar energy, thermophotovoltaics, infrared imaging, and thermal emission^{29–33}. Usually, they are made of three standard layers of metal-dielectric-metal based configuration. The intermediate dielectric spacers divide top and bottom plasmonic metals into metamaterial absorbers, which are made at the nanoscale subwavelength level.

Traditionally, plasmonic metals such as aluminum, gold, and silver were used in the designing of nanostructured absorbers due to their ability to support strong surface plasmon resonances in the visible and near-infrared spectrum. These metals exhibit low intrinsic losses at optical frequencies and offer well-characterized, stable plasmonic behavior, making them ideal for many applications in sensing, photovoltaics, and photodetection. These traditional plasmonic metals suffer from high reflectivity and limited tunability at higher frequencies (e.g., mid infrared to terahertz), poor thermal stability especially in the case of gold and silver, and material compatibility issues when integrated with CMOS platforms. To create effective and affordable wideband absorbers at the nanoscale, scientists are looking for alternative options of various available metals like tungsten, nickel, chromium and titanium due to their higher melting points and large absorption capabilities. In this scenario, numerous kinds of plasmonic metasurface absorbers were investigated from the last couple of years for diverse applications. Hoa et al. presented a high bandwidth nanostructured metasurface absorber

¹Department of Electrical Engineering, College of Engineering, Jouf University, Sakaka 72388, Saudi Arabia. ²School of Engineering and Physical Sciences, Institute of Sensors, Heriot Watt University Edinburgh, Edinburgh, UK. [™]email: mmaalsharari@ju.edu.sa

which covers the large wavelength band starting from visible to infrared³⁴. Within the visible light spectrum, another nanoscale absorber described in⁹, which contained an elliptical concentric ring of tungsten showed an absorption threshold of over 90%. Similarly, the entire visible light spectrum was covered by designing the simple chromium-based metasurface absorber³⁵. Moreover, there are numerous design combinations that use nickel metal in the designing of nanostructured absorbers which cover visible to infrared wavelengths^{10,36,37}. A new family of nitride metals is currently receiving more attention to design and explore nanostructured absorbers, specifically suited for use in thermophotovoltaics and solar cells^{29,38,39}. These metal nitrides have high melting points, which make them suitable for high-temperature applications. Several well-known transition metal nitrides, including ZrN, TiN, VN and HfN, provide the possibility to explore wideband nanostructured absorbers specifically used for solar cell and thermophotovoltaic applications^{40–42}. When it comes to mechanical stability, thermal resistance, and CMOS compatibility, these metal nitrides stand apart from other metals that are currently on the market^{43,44}.

The main purpose of this work is to employ the HfN in the design and analysis of a nanostructured absorber. This work uses a straightforward, simple and easily fabricable nano circular ring made of HfN as a broadband absorber that targets infrared wavelengths with an absorption threshold of 90%. The suggested HfN metasurface absorber exhibits a large optical bandwidth within the wavelength spectrum from 700 to 1700 nm. By adjusting the incident angles of the incoming light, the designed HfN absorber shows good absorption properties, and even at θ = 60°, the average absorption value of over 70% is noticed. The performance of this metasurface absorber is analyzed under varying polarization angles, and it is found to be insensitive to changes in polarization of an incoming optical light. It has potential for usage in solar cells and thermophotovoltaics due to its wider bandwidth, mechanical stability, and thermal durability.

Design method and HfN absorber simulation

In this section, the design and simulation setup of the HfN metasurface absorber is presented. Figure 1 presents the top view of the unit cell, along with the 3D arrangement of its array pattern. The thermally resistant transition metal of HfN is used as a top and bottom layer in the designing of a metasurface absorber, with a silicon dielectric layer placed between them to trap the optical light inside the cavity. The value of the silicon dielectric permittivity (ε_*) and loss tangent $(\tan \delta)$ are considered 2.25 and 0.0003 in the simulation study respectively.

The optimal unit cell of the HfN metasurface absorber along with its final geometric parameters are labelled in Fig. 1a, and the associated values are given as follows: $R_{out} = 130$, $R_{in} = 60$, $h_s = 120$, t = 40, and with P = 300. All the units of these parameters are considered in nm.

The EM solver CST is employed to model, design and simulate the unit cell of the HfN metasurface absorber. The frequency domain solver is employed to simulate the basic unit cell of the absorber. The frequency domain solver uses the floquet theorem which considers the single unit cell as a periodic array of the used elements. The metasurface absorber is excited from the positive z-direction and remained open in negative z-axis. Furthermore, the unit cell boundary conditions are used in both the x-y direction.

Simulation results and discussion

Firstly, the value of the real and imaginary parts of the permittivity of the HfN material is extracted and presented in Fig. 2. To have a look into the scattering features of the HfN absorber, an incident light with normal direction (θ =0°) is first used as the input wave. Figure 3 shows the equivalent characteristics of the suggested HfN absorber. To get insight into the absorption properties, we first extract the S_{11} parameter and normalized impedance of the suggested HfN absorber, as seen in Fig. 3a.

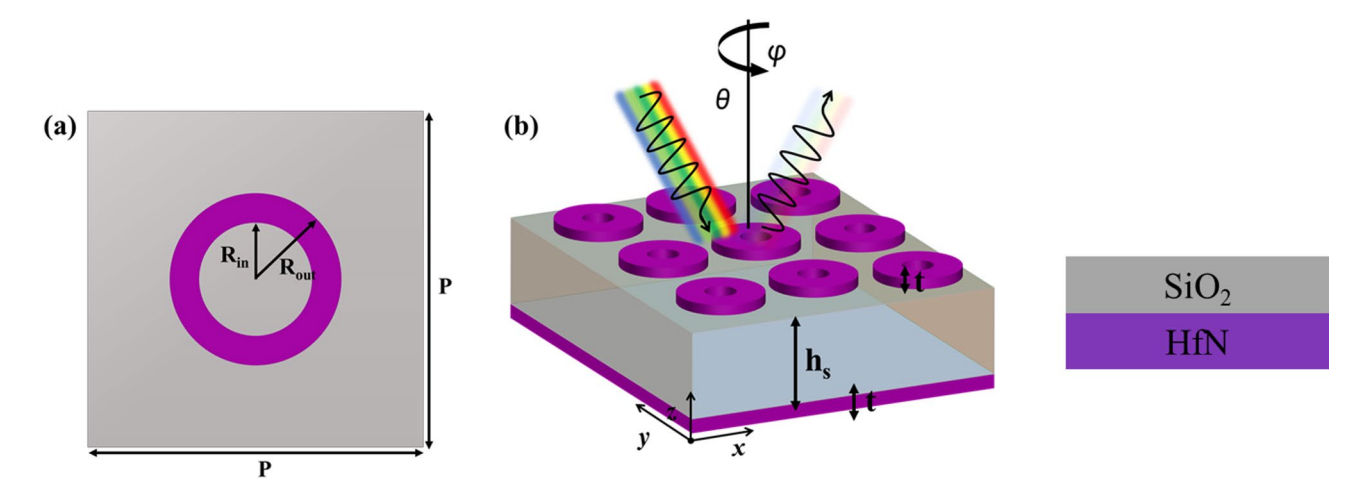


Fig. 1. (a) Presentation of the unit element of the HfN metasurface-based absorber. (b) Highlighting 3D unit elements array of the HfN metasurface-based absorber. This 3D image is created by the authors using Microsoft PowerPoint (Microsoft 365, Version 2507, Microsoft Corporation).

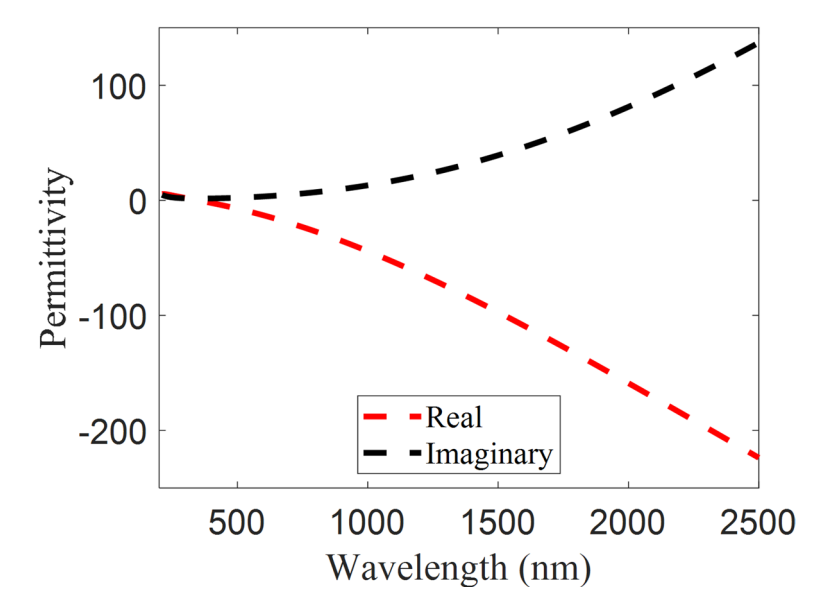


Fig. 2. Real and imaginary components of the permittivity of the HfN.

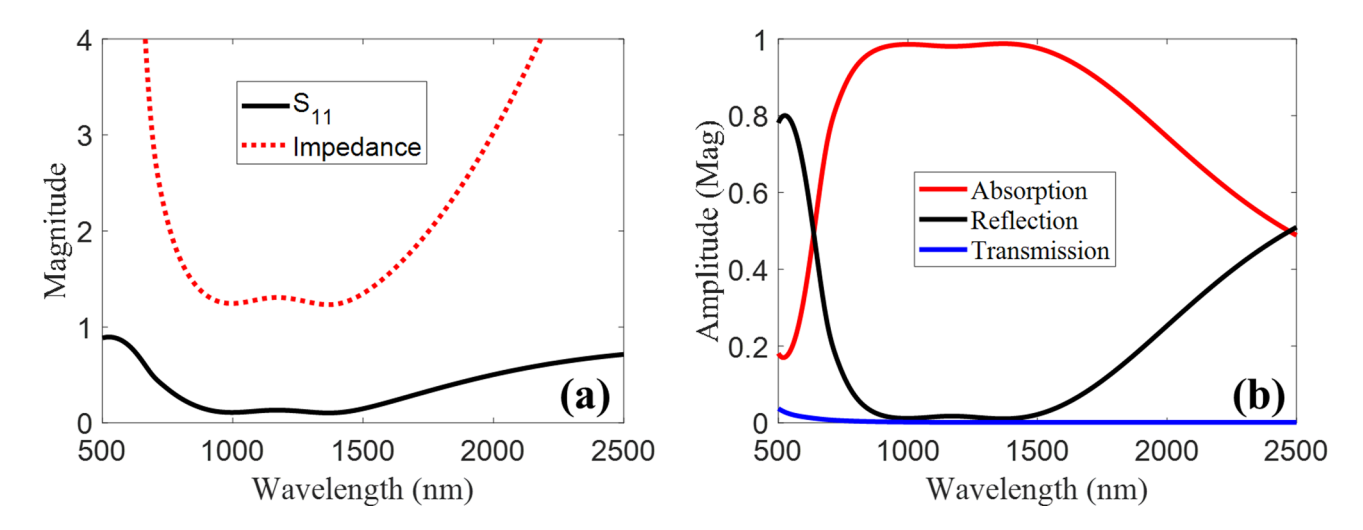


Fig. 3. (a) Normalized impedance- S_{11} of the proposed HfN metasurface absorber and (b) scattering parameters of the proposed HfN metasurface absorber.

The absorber under discussion has an S_{11} component that indicates a value of 0.3 within the intended wavelength range of 700 nm to 1700 nm. This indicates that the absorption is acceptable. Perfect absorption requires a normalized impedance of unity, which is a crucial parameter to verify the impedance matching conditions. The normalized impedance in Fig. 3(a) is shown to revolve around 1.5, indicating satisfactory impedance matching. The normalized impedance presented in Fig. 3(a) refers to the effective impedance ($Z_{\rm eff}$) of the metamaterial structure, normalized with respect to the impedance of free space (Z_0 = 377 Ω). This normalized impedance is calculated using the standard retrieval method from simulated S-parameters, typically given by 10 :

$$Z_{eff} = Z_0 \sqrt{\frac{1 + S_{11}^2 - S_{21}^2}{1 - S_{11}^2 - S_{21}^2}} \tag{1}$$

In our case, the value revolves around 1.5, meaning the effective impedance is approximately $Z_{\rm eff}=1.5\times377=565.5$ Ω . In practical metamaterial and absorber design, perfect matching to free space (Z/Z0=1) is ideal, but slight deviations (e.g., 1.2–1.8) are often acceptable, especially when minimal reflection is observed. In our case, the reflection coefficient S_{11} remains low in the operational band, indicating minimal impedance mismatch. The normalized impedance revolving around 1.5 still ensures that the real part of the impedance dominates and the imaginary component is small near resonance, allowing for good absorption and energy transfer into the structure.

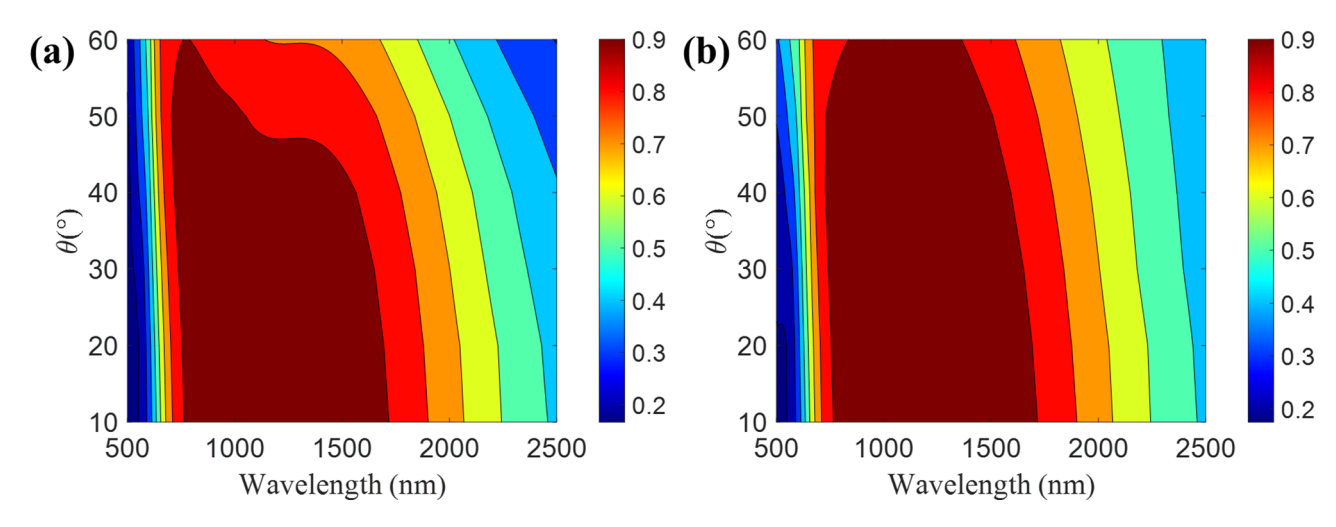


Fig. 4. (a) TE wave excitation for various incident angles and (b) TM wave excitation for various incident angles.

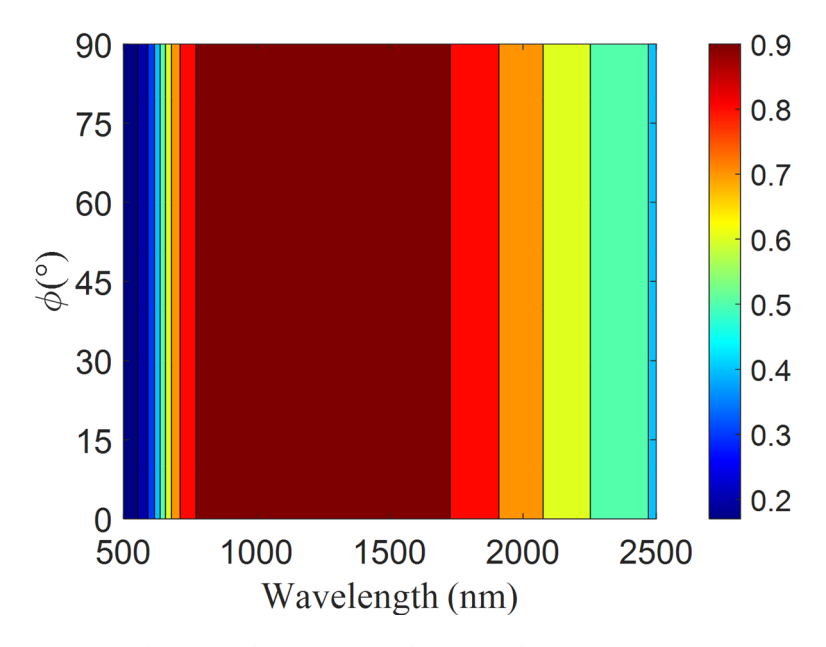


Fig. 5. Performance of the designed HfN metasurface absorber under various polarization angles.

The associated absorption characteristics of the design HfN absorber are shown in Fig. 3(b). Notably, its average absorption is greater than 90% within the operating wavelength range of 700 nm to 1700 nm.

The developed HfN absorber exhibits omni-directional properties, including polarization insensitivity and angular sensitivity. The intended absorber's absorption characteristics are investigated for this purpose by varying θ between 10° and 60°. Figure 4a illustrates the equivalent absorption for the excitation of the TE mode, and Fig. 4b shows the absorption for the polarization of the TM wave.

Initially, let's consider the scenario where θ ranges from 10° to 30°. In this case, the suggested absorber provides comparable absorption features while barely reducing the absorption characteristics. A little decrease in total absorption was noted when θ = 40°, while the absorption bandwidth is still quite acceptable. At θ = 50°–60°, the absorption finally started to decline, but for this range of oblique angles, the total absorption remained over 70%. Notably, compared to the TE mode wave polarization, there is no noticeable decrease in absorption for the TM mode excitation.

Metamaterial absorber polarization insensitivity to the interaction of any incident polarized optical light is yet another important characteristic. The metamaterial absorber must be strong enough to carry out the polarization insensitive function since the entering optical light may be in any polarization state. To detect this feature, we vary the ϕ by 30 increments from 0° to 90°. The related absorption characteristics are shown in Fig. 5, and it has the same absorption characteristics for all ϕ , as shown in Fig. 5. This unique and crucial ability of the absorber to capture all polarization states of optical light is due to its four-fold symmetrical design.

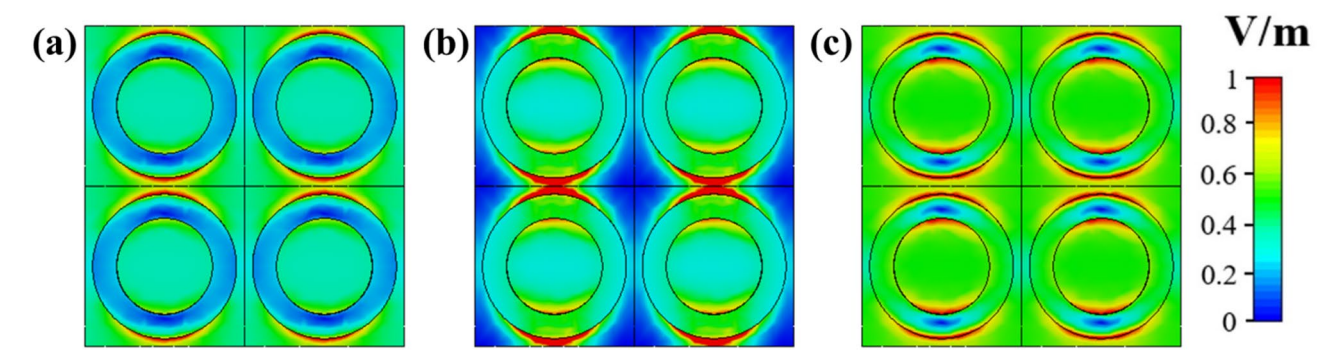


Fig. 6. Electric field distribution of the designed HfN metasurface absorber at three operating points: (a) = 700 nm, (b) = 1200 nm, and (c) = 1700 nm.

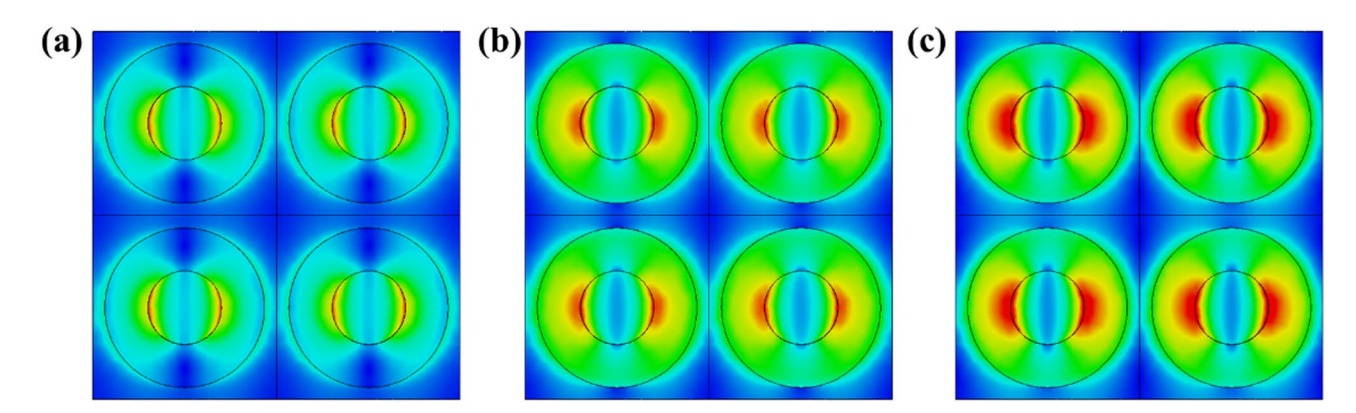


Fig. 7. Magnetic field distribution of the designed HfN metasurface absorber at three operating points: (a) = 700 nm, (b) = 1200 nm, and (c) = 1700 nm.

Moreover, the suggested HFN-based absorber's electric field analysis is provided, which aids in a better comprehension of the physical interpretation of the absorption phenomena. We deliberately chose three working wavelength points: 700 nm, 1200 nm, and 1700 nm, to detect the electric field.

Figure 6 shows the matching intensity distributions. The electric field pattern at the lower wavelength of 700 nm is shown in Fig. 6a, with the lower and upper portions of the circular nano-ring exhibiting the lowest intensity. As demonstrated in Fig. 6b, it is also evident that, at 1200 nm, the electric field intensity is primarily concentrated around the top and bottom portions of the nano-ring resonator. It is important to observe that the e-field's intensity is lower at the lower wavelength of 700 nm than the higher wavelength point of 1200 nm. This is because 1200 nm is the wavelength at which absorption is at its highest value. Furthermore, the electric field distribution is somewhat higher at = 1700 nm than at = 700 nm due to the higher absorption value at this location, as seen in Fig. 6c.

This result confirms that absorption occurs mostly at the upper and lower corners of the circular resonator at this wavelength range. For this reason, a ring with a circular shape is essential in greatly increasing the total absorption efficiency. Because of this, the circular-shaped ring plays a crucial role in significantly raising overall absorption efficiency. The absorption efficiency is greatly improved by these three plasmonic resonances. The electric field distribution confirms strong localization at the upper and lower edges of the ring, indicating excitation of surface plasmon resonances. These resonances are wavelength-dependent, and different modes, such as dipolar, quadrupolar, or higher-order plasmonic modes can be excited at varying wavelengths. In our design, multi-mode resonance is obtained by engineering geometric features like ring width, thickness, and periodicity, which tailor the resonance conditions across a broad spectral range. This leads to overlapping absorption peaks and enables broadband performance.

Additionally, for wavelengths of 700 nm, 1200 nm, and 1700 nm, the magnetic field distributions at the surface of the circular ring-shaped HfN absorber show distinct resonance behaviors, as shown in Fig. 7. At 700 nm (a), the magnetic field is strongly confined within the ring structure, indicating a well-localized magnetic dipole resonance. As the wavelength increases to 1200 nm (b), the field begins to spread outward, suggesting a broader resonance or the excitation of higher-order modes. At 1700 nm (c), the magnetic field becomes more delocalized, with strong dipolar patterns forming on both sides of the ring. This indicates hybrid or collective resonances across the array, contributing to broadband absorption performance. The evolution of the magnetic field profile with wavelength highlights the role of resonance shifting and field coupling in the absorber's optical response.

Additionally, the absorption characteristics of the proposed absorber are also investigated by employing various types of dielectric spacer by keeping all the geometric parameters remaining same. For this scenario, we employ different available dielectric materials such as AlN (ϵ_r = 8.6), GaAs (ϵ_r = 12.94), Si (ϵ_r = 11.9) and Al₂O₃ (ϵ_r = 9.85) etc. Figure 8 highlights the absorption trend of the proposed absorber when different spacers are used. It is observed that for all dielectric spacers, the absorber exhibits a dual-band response in both the visible and infrared regions. However, when SiO₂ is used, it covers a broader absorption spectrum, ranging from 700 to 1700 nm. Additionally, the full width half maximum (FWHM) of each absorption curve is calculated to quantify the spectral bandwidth of the peak. Since the analysis extends up to 2500 nm and all curves maintain absorption values above 0.5 beyond this wavelength, 2500 nm was selected as the upper limit for FWHM estimation. Based on this condition, the FWHM values are calculated as follows: 957 nm for Si, 1225 nm for AlN, 877 nm for GaAs, 1118 nm for Al₂O₃, and 1840 nm for SiO₂.

Furthermore, engineering the absorption of bandwidth is significantly influenced by the design parameters of the proposed HfN-based absorber. Thus, considering the most important and crucial design factors that would aid in optimizing the absorption properties, we conducted a parametric study of the suggested HfNbased absorber. For this reason, we considered various design parameters including dielectric thickness, unit cell periodicity, outer and inner radius of the top meta-unit cell. Initially, we tuned the dielectric thickness from 80 nm to 160 nm and the corresponding absorption results are highlighted in Fig. 9a. At h_e = [80 100] nm, the absorption values decrease at higher operating wavelengths, and the trend begins to flatten as the h value increases. Figure 9b shows the absorption trend as the periodicity of the unit cell is varied. The proposed absorber performs poorly at P = 260 nm, and it shows very poor absorption features. However, when P is increased to 280 nm and 300 nm, it demonstrates a broader absorption bandwidth, as indicated by the blue and red lines. At P = [320 340], the absorber still exhibits good absorption, but its bandwidth begins to narrow. Moreover, we also inspect the absorption features of the proposed absorber under the variation inner and outer radii of the participating nano-ring. We changed the outer radius (R_{out}) with a step size of 10 nm, observing the effects. The corresponding absorption features are shown in Fig. 9c. It is shown that as we raise the value of R_{out}, the absorption gradually starts to improve at higher wavelengths while remaining flattens for $R_{out} = 130$ nm. As illustrated in Fig. 9d, we also examine the absorption trend under the influence of the inner radius (R_{in}) with a step size of 10 nm, going from 30 nm to 70 nm. The suggested absorber exhibits similar absorption trend when we vary the $R_{\rm in}$ from 30 nm to 70 nm, but it displays a respectable absorption value at $R_{\rm in} = 60$ nm. Ultimately, the absorber's absorption characteristics can be significantly altered by varying its design parameters.

Multi-reflection interference theory

The analytical model based on multi-reflection phenomena, as shown in Fig. 10, is presented to observe the transmitted and reflected waves between the top surface and the ground plane. The periodic FSS arrays at the

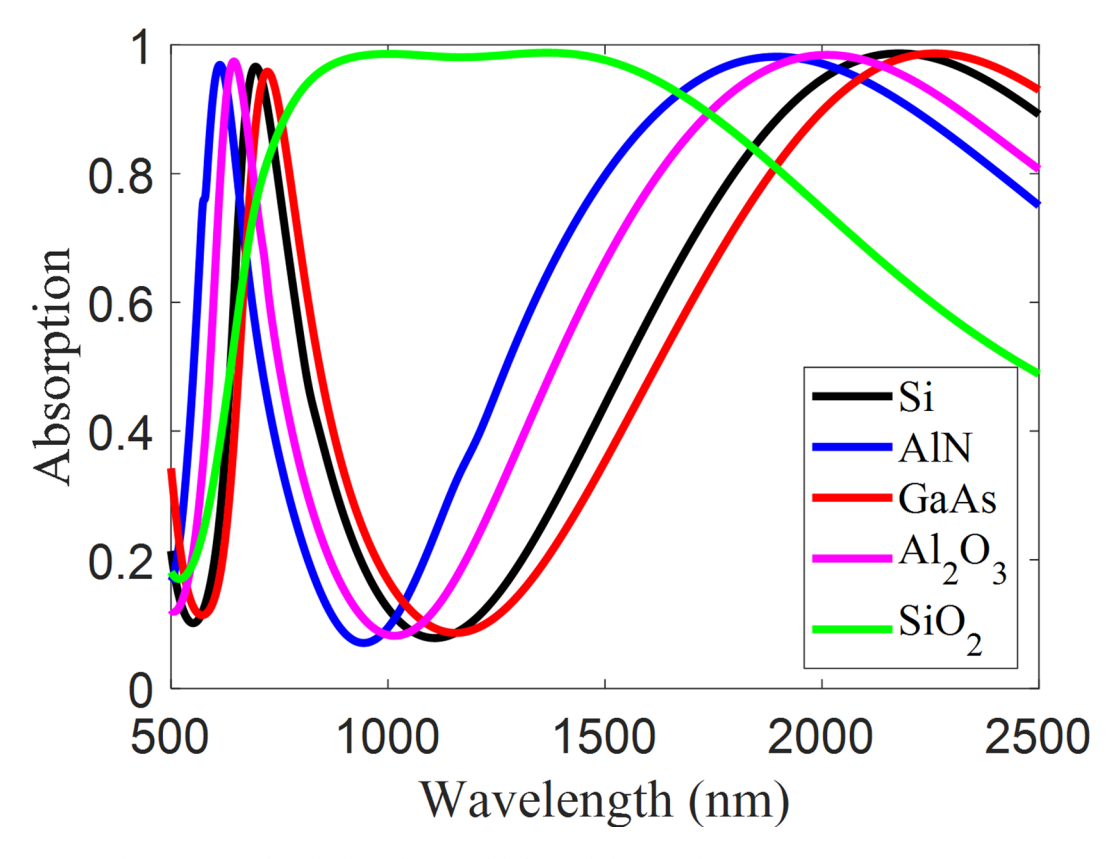


Fig. 8. Absorption trend under the influence of different dielectric substrates.

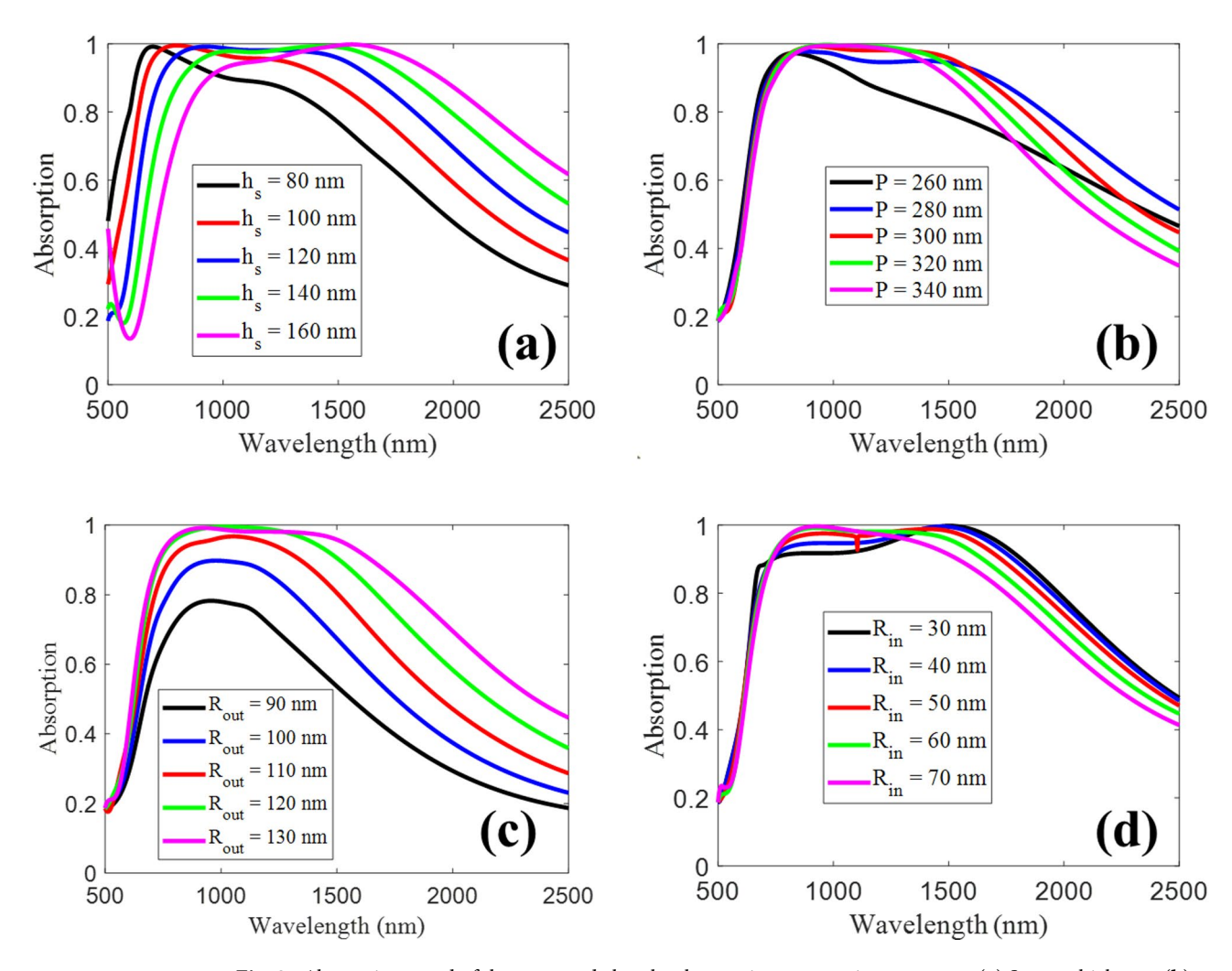


Fig. 9. Absorption trend of the proposed absorber by varying geometric parameters (a) Spacer thickness, (b) Unit cell periodicity, (c) Outer radius and (d) Inner radius.

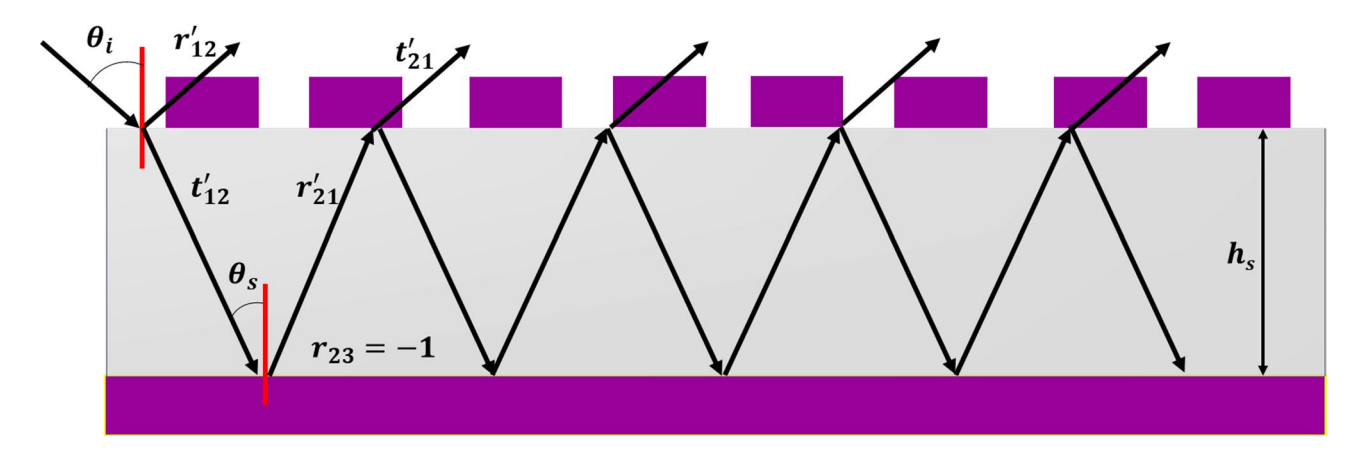


Fig. 10. Analytical interference cavity model based on multi-reflection theory of the designed HfN metasurface absorber.

top are used as impedance surfaces, and the lower ground serves as a perfect reflector. Impedance matching allows EM waves to enter the spacer as they get closer to the upper periodic arrays. The dielectric spacer then experiences several reflection phenomena, as seen in Fig. 10. They relate to the following mathematical quantities, which are expressed as: $r'_{12} = r_{12}e^{i\Phi_{~12}}$ and $t'_{12} = t_{12}e^{i\Phi_{~12}}$. Upon encountering the lower ground reflector,

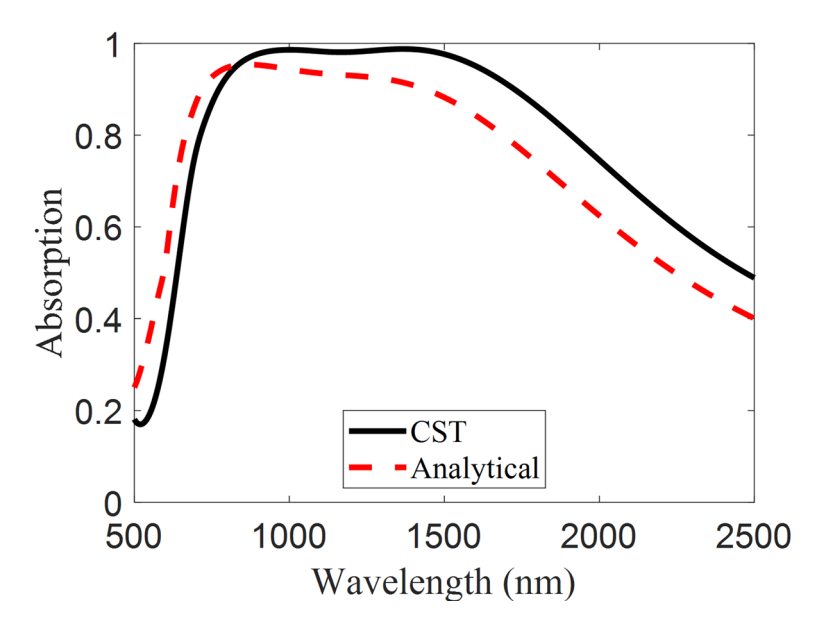


Fig. 11. Comparative analysis between the absorption features of the suggested HfN which are calculated through CST simulation and analytical interference theory method.

Absorber design	Used material	Absorber layers	Bandwidth	Stability	Polarization-independent
Fractal ellipses ⁹	W, SiO ₂	3	400-750 nm	$\theta_i = 60^{\circ}$	No
Concentric Triangular-rings ³¹	Cr, SiO ₂	3	400-750 nm	$\theta_i = 60^{\circ}$	Yes
Nano-disk array ³⁹	HfN, SiO ₂	3	500-1100 nm	$\theta_i = 60^{\circ}$	Yes
Crosses array ⁴⁸	HfN, SiO ₂	3	300-800 nm	$\theta_i = 60^{\circ}$	Yes
Nano-cylinders ⁴⁹	Ni	3	400-650 nm	$\theta_i = 60^{\circ}$	Yes
Circular ring (This work)	HfN, Si	3	700–1700 nm	$\theta_i = 60^{\circ}$	Yes

Table 1. Comparative analysis of the proposed HfN absorber with the existing absorber designs.

the transmitted component reflects, resulting in a complicated propagation phase and a reflection amplitude of -1 to the dielectric spacer. $\beta=nk_oh_s$, Here h_s shows the height of the dielectric substrate and k_o represents the free-space wavenumber. Again, there is a partial transmission-reflection phenomena that occur with related energy levels of $t_{21}'=t_{21}e^{i\Phi}$ t_{21} and $t_{21}'=r_{21}e^{i\Phi}$ t_{21} , respectively. Due to these interactions, a destructive interference takes place inside this cavity and ultimately, the total reflection of the system can be computed as 46,47. The multiple reflection interference theory used assumes ideal conditions like infinite planar layers and homogeneous media for analytical simplicity. In practice, edge effects and material inhomogeneities can affect performance, but these are minimized by subwavelength unit cells and large arrays.

$$r = r'_{12} - \frac{t'_{12}t'_{21}e^{i2\beta}}{1 + r'_{21}e^{i2\beta}}$$
 (2)

The related analytical absorption of the suggested HfN absorber can be evaluated by utilizing $A=1-|r|^2$. The computed analytical and the full-wave simulation absorption have been compared to demonstrate the compatibility between the two. A comparison of the simulated and estimated absorption is shown in Fig. 11, where a close alignment is observed.

A detailed comparative study of the various existing absorber design is presented in Table 1. In our work, a circular-shaped unit cell was chosen due to its simple geometry, which allows easy fabrication using standard lithography techniques. In contrast to the design in³⁹, which used a 3×3 array of nano-disks and achieved broadband absorption from 500 nm to 1100 nm, our design uses a single circular ring-shaped unit cell and demonstrates a much broader absorption bandwidth from 700 nm to 1700 nm. The geometric parameters of our absorber were fully optimized to achieve this wideband performance. While further bandwidth enhancement is possible using multi-layer designs, our goal was to create a single-layer, ultrathin, and low-profile absorber.

Unlike many visible and infrared absorbers that rely on complex multi-layer structures, our single-layer design simplifies fabrication, lowers cost, and is more suitable for integration into advanced photonic systems. Additionally, the structure's four-fold symmetry ensures polarization-insensitive performance.

Material	Absorption efficiency	Melting point (°C)	Mechanical hardness (GPa)	Thermal stability	Oxidation resistance
HfN	High (broadband, tunable)	~ 3310	~23-25	Excellent ³⁹	High (forms HfO2 layer)
Au	High (narrowband)	~ 1064	~ 2.5	Poor ⁴¹	Low
Ag	Very high (narrowband)	~962	~2.5	Poor ⁴¹	Very low
Al	Moderate	~ 660	~1-3	Low ⁵⁰	Moderate
W	Good	~ 3422	~15-20	Excellent ⁹	Moderate
Ni	High	~ 1455	~5-7	Moderate ¹⁰	Moderate
TiN	High	~ 2950	~20-22	High ⁵¹	High

Table 2. Comparison of HfN with common plasmonic metals in terms of absorption performance, mechanical stability, and thermal stability for infrared absorber applications.

Material	Stability in harsh environments	Remarks		
HfN	Very stable in air and under thermal cycles	Excellent mechanical and thermal durability		
Ni	Moderate; surface oxidation common	Needs passivation for long-term use		
Cr	Stable under moderate thermal cycling	Often used in harsh environments		
W	High stability, but heavy	Brittle in thin films		
Au	Degrades under heat and pressure	High conductivity but poor durability		
Ag	Not suitable for harsh conditions	Needs protective coating		
Al	Surface oxide protects but reduces plasmonic performance	Common but less stable		

Table 3. Environmental stability of HfN vs. other plasmonic materials.

Material stability and comparative performance analysis

This section discusses material stability, thermal compatibility, mechanical robustness, environmental suitability, and other performance parameters of various existing plasmonic metals, and compares them with HfN. Detailed performance and comparative analyses are presented in Tables 2 and 3.

Fabrication feasibility of HfN absorber

Various fabrication techniques have been employed to develop nanostructured absorbers. In this work, we present two commonly used methods to demonstrate the fabrication feasibility of the proposed absorber.

For fabrication, a standard photolithography process in a cleanroom environment can be employed. Hafnium nitride (HfN) layers are first deposited onto a silicon wafer using electron-beam evaporation. A photoresist is then spin-coated onto the substrate, and the desired patterns are transferred from a photomask to the photoresist via UV exposure, followed by development. Thanks to the scalability of photolithography, the patterns can be reliably produced over a relatively large area. Subsequently, the sample undergoes etching with argon gas in an inductively coupled plasma (ICP) system, using the patterned photoresist as a mask. Finally, the photoresist is removed using a stripper solution, resulting in the desired pattern being etched into the HfN layer⁵².

HfN can be readily deposited and patterned using electron-beam evaporation and electron-beam lithography. Alternatively, nanoimprint lithography (NIL) or roll-to-roll imprinting can be employed to fabricate HfN-based absorbers over large areas, enabling high-throughput production. These HfN metamaterial absorbers can be integrated on silicon substrates, allowing compatibility with silicon-based electronic and photonic components, including photonic chips.

The fabrication steps using the NIL technique are outlined as follows: First, thin films of HfN and silica are deposited onto a silicon substrate via electron-beam evaporation. A polymethyl methacrylate (PMMA) resist layer is then spin-coated and baked. To mitigate charge accumulation on the silica surface during patterning, a conductive polymer layer is spin-coated on top of the resist. Electron-beam lithography is used to expose the desired patterns onto the resist. After exposure, the conductive polymer layer is removed with deionized (DI) water, and the exposed photoresist is developed. Finally, a thick HfN layer is deposited by electron-beam evaporation, and the circular-shaped patterns are transferred onto the substrate³⁵.

Conclusion

In conclusion, the design and analysis of a nanoscale metasurface absorber for short-infrared wavelength spectrum made use of the transition metal HfN was presented. The middle dielectric spacer was positioned between the upper and bottom HfN layers in the proposed design of the absorber. The top HfN layer was made of a simple and straightforward circular nano-ring which is a basic building block for impedance adjustment of the absorber. With an absorption rate of 90%, the suggested HfN absorber showed a reasonable absorption optical bandwidth from 700 to 1700 nm. Additionally, this absorber exhibited polarization-insensitive behavior owing to the presence of symmetric geometry of the top nano-ring. It also showed an overall value of more than 70% and retained its absorption characteristics at oblique angles up to 60°. Lastly, the multi-reflection theory was implemented to validate the full-wave simulation results. It has potential uses in thermophotovoltaics and solar cells because of its strong absorption response, ultracompact geometry, cost-effectiveness, and thermal stability.

Data availability

The data supporting the findings in this work are available from the corresponding author with a reasonable request.

Received: 24 February 2025; Accepted: 18 August 2025

Published online: 26 September 2025

References

- 1. Engheta, N. & Ziolkowski, R. W. Metamaterials: Physics and Engineering Explorations (Wiley, 2006).
- 2. Bilal, R. et al. A novel Omega shaped microwave absorber with wideband negative refractive index for C-band applications. *Optik* **242**, 167278 (2021).
- Grant, J., Kenney, M., Shah, Y. D., Escorcia-Carranza, I. & Cumming, D. R. CMOS compatible metamaterial absorbers for hyperspectral medium wave infrared imaging and sensing applications. Opt. Express. 26 (8), 10408–10420 (2018).
- 4. Khorasaninejad, M. et al. Multispectral chiral imaging with a Metalens. Nano Lett. 16 (7), 4595-4600 (2016).
- 5. Bilal, R., Baqir, M., Choudhury, P., Ali, M. & Rahim, A. Tunable and multiple plasmon-induced transparency in a metasurface comprised of silver s-shaped resonator and rectangular strip. *IEEE Photonics J.* **12** (3), 1–13 (2020).
- 6. Yang, W. & Lin, Y. S. Tunable metamaterial filter for optical communication in the Terahertz frequency range. Opt. Express. 28 (12), 17620–17629 (2020).
- 7. Armghan, A., Abdulrazak, L. F., Baqir, M. A., Saqlain, M. & Al-Shammari, H. Multiband, polarization-insensitive absorber operating in the Terahertz range. *J. Comput. Electron.* 1–7 (2024).
- 8. Tang, H. et al. Rational design of high-performance epoxy/expandable microsphere foam with outstanding mechanical, thermal, and dielectric properties. J. Appl. Polym. Sci. e55502 (2024).
- 9. Bilal, R. et al. Elliptical metallic rings-shaped fractal metamaterial absorber in the visible regime. Sci. Rep. 10 (1), 14035 (2020).
- Naveed, M. A. et al. Ultrawideband fractal metamaterial absorber made of nickel operating in the UV to IR spectrum. Opt. Express. 29 (26), 42911–42923 (2021).
- 11. Yu, N. & Capasso, F. Flat optics with designer metasurfaces. Nat. Mater. 13 (2), 139-150 (2014).
- 12. Liu, Y. & Zhang, X. Metamaterials: a new frontier of science and technology. Chem. Soc. Rev. 40 (5), 2494-2507 (2011).
- 13. Shalaev, V. M. Optical negative-index metamaterials. Nat. Photonics. 1 (1), 41-48 (2007).
- 14. Smith, D. R., Pendry, J. B. & Wiltshire, M. C. Metamaterials and negative refractive index. Science 305(5685), 788-792 (2004).
- 15. Garg, P. & Jain, P. Isolation improvement of MIMO antenna using a novel flower shaped metamaterial absorber at 5.5 ghz wimax band. *IEEE Trans. Circuits Syst. II Express Briefs.* **67** (4), 675–679 (2019).
- 16. Alsulami, Q. A., Wageh, S., Al-Ghamdi, A. A., Bilal, R. M. H. & Saeed, M. A. A Tunable and Wearable Dual-Band Metamaterial Absorber Based on Polyethylene Terephthalate (PET) Substrate for Sensing Applications. *Polymers* 14(21), 4503 (2022).
- 17. Bilal, R. & Naveed, M. A comment: a set square design metamaterial absorber for X-band applications. J. Electromagn. Waves Appl. 35 (10), 1354–1358 (2021).
- 18. Huang, X. et al. Simultaneous realization of polarization conversion for reflected and transmitted waves with bi-functional metasurface. Sci. Rep. 12 (1), 2368 (2022).
- 19. Li, Z., Liu, W., Cheng, H., Chen, S. & Tian, J. Realizing broadband and invertible linear-to-circular polarization converter with ultrathin single-layer metasurface. Sci. Rep. 5 (1), 18106 (2015).
- 20. Zhu, H., Cheung, S., Chung, K. L. & Yuk, T. I. Linear-to-circular polarization conversion using metasurface. *IEEE Trans. Antennas Propag.* 61 (9), 4615–4623 (2013).
- 21. He, X. et al. Excellent microwave absorption performance of LaFeO3/Fe3O4/C perovskite composites with optimized structure and impedance matching. *Carbon* 213, 118200 (2023).
- 22. Yoo, M., Kim, H. K. & Lim, S. Electromagnetic-based ethanol chemical sensor using metamaterial absorber. Sens. Actuators B. 222, 173–180 (2016).
- 23. Li, T. et al. Integrating the optical tweezers and spanner onto an individual single-layer metasurface. *Photonics Res.* **9** (6), 1062–1068 (2021).
- 24. Li, Z. et al. Hybrid metasurface-based mid-infrared biosensor for simultaneous quantification and identification of monolayer protein. Acs Photonics. 6 (2), 501–509 (2019).
- Bilal, R. M. H. et al. Nanoengineered nickel-based ultrathin metamaterial absorber for the visible and short-infrared spectrum. Opt. Mater. Express. 13 (1), 28–40 (2023).
- 26. Zakir, S. et al. Polarization-insensitive, broadband, and tunable Terahertz absorber using slotted-square graphene meta-rings. *IEEE Photonics J.* 15 (1), 1–8 (2022).
- 27. Bilal, R. M. H. et al. Wideband microwave absorber comprising metallic split-ring resonators surrounded with E-shaped fractal metamaterial. *IEEE Access.* **9**, 5670–5677 (2021).
- 28. Zhang, G. et al. Electrically assisted continuous vat photopolymerization 3D printing for fabricating high-performance ordered graphene/polymer composites. *Compos. Part. B: Eng.* 250, 110449 (2023).
- 29. Liu, Z., Liu, G., Huang, Z., Liu, X. & Fu, G. Ultra-broadband perfect solar absorber by an ultra-thin refractory titanium nitride meta-surface. Sol. Energy Mater. Sol. Cells. 179, 346–352 (2018).
- 30. Mehrabi, S., Bilal, R. M. H., Naveed, M. A. & Ali, M. M. Ultra-broadband nanostructured metamaterial absorber based on stacked square-layers of tin/tio 2. Opt. Mater. Express. 12 (6), 2199–2211 (2022).
- 31. Bilal, R. M. H., Baqir, M. A., Hameed, M., Naqvi, S. A. & Ali, M. M. Triangular metallic ring-shaped broadband polarization-insensitive and wide-angle metamaterial absorber for visible regime. *JOSA A.* **39** (1), 136–142 (2022).
- 32. Bilal, R. et al. Ultrathin broadband metasurface-based absorber comprised of tungsten nanowires. Res. Phys. 19, 103471 (2020).
- 33. Armghan, A. et al. Performance optimization of energy-efficient solar absorbers for thermal energy harvesting in modern industrial environments using a solar deep learning model. *Heliyon* (2024).
- 34. Hoa, N. T. Q., Lam, P. H., Tung, P. D., Tuan, T. S. & Nguyen, H. Numerical study of a wide-angle and polarization-insensitive ultrabroadband metamaterial absorber in visible and near-infrared region. *IEEE Photon. J.* 11 (1), 1–8 (2019).
- 35. Kim, I., So, S., Rana, A. S., Mehmood, M. Q. & Rho, J. Thermally robust ring-shaped chromium perfect absorber of visible light. *Nanophotonics* 7(11), 1827–1833 (2018).
- 36. Hakim, M. L. et al. Ultrawideband polarization-independent nanoarchitectonics: a perfect metamaterial absorber for visible and infrared optical window applications. *Nanomaterials* 12(16), 2849 (2022).
- 37. Qian, Q., Yan, Y. & Wang, C. Flexible metasurface black nickel with stepped nanopillars. Opt. Lett. 43 (6), 1231–1234 (2018).
- 38. Sheta, E., Choudhury, P. & Ibrahim, A. B. M. Polarization-insensitive ultra-wideband metamaterial absorber comprising different forms of ZrN structures at the metasurface. *Opt. Mater.* 133, 112990 (2022).
- Sheta, E. & Choudhury, P. K. Nanoengineered hafnium nitride hyperbolic metasurface based polarization insensitive UWB absorber. IEEE Photonics Technol. Lett. 33 (24), 1351–1354 (2021).
- 40. Naik, G. V., Kim, J. & Boltasseva, A. Oxides and nitrides as alternative plasmonic materials in the optical range. *Opt. Mater. Express.* 1 (6), 1090–1099 (2011).

- 41. Naik, G. V., Shalaev, V. M. & Boltasseva, A. Alternative plasmonic materials: beyond gold and silver, *Adv. Mater.* 25(24), 3264–3294 (2013).
- 42. West, P. R. et al. Searching for better plasmonic materials. Laser Photonics Rev. 4 (6), 795-808 (2010).
- 43. Dong, S., Chen, X., Zhang, X. & Cui, G. Nanostructured transition metal nitrides for energy storage and fuel cells. *Coord. Chem. Rev.* 257, 13–14 (2013).
- 44. Gosciniak, J., Atar, F. B., Corbett, B. & Rasras, M. Plasmonic Schottky photodetector with metal Stripe embedded into semiconductor and with a CMOS-compatible titanium nitride. Sci. Rep. 9 (1), 6048 (2019).
- 45. Gueddaoui, H., Maabed, S., Schmerber, G., Guemmaz, M. & Parlebas, J. Structural and optical properties of vanadium and hafnium nitride nanoscale films: effect of stoichiometry. Eur. Phys. J. B. 60, 305–312 (2007).
- 46. Chen, H. T. Interference theory of metamaterial perfect absorbers. Opt. Express. 20 (7), 7165-7172 (2012).
- 47. Chen, J. et al. High-impedance surface-based broadband absorbers with interference theory. *IEEE Trans. Antennas Propag.* **63** (10), 4367–4374 (2015).
- 48. Shafique, A. et al. Highly efficient vanadium nitride based metasurface absorber/emitter for solar-thermophotovoltaic system. Mater. Today Commun. 34, 105416 (2023).
- 49. Zhou, Y. et al. Cost-effective near-perfect absorber at visible frequency based on homogenous meta-surface nickel with two-dimension cylinder array. Opt. Express. 26 (21), 27482–27491 (2018).
- 50. Knight, M. W. et al. Aluminum for plasmonics. ACS Nano. 8 (1), 834-840 (2014).
- 51. Reddy, H. et al. Temperature-dependent optical properties of plasmonic titanium nitride thin films. ACS Photonics. 4 (6), 1413–1420 (2017).
- 52. Liu, J. et al. Wafer-scale metamaterials for polarization-insensitive and dual-band perfect absorption, *Nanoscale* 7(45), 18914–18917 (2015).

Acknowledgements

This work was funded by the Deanship of Graduate Studies and Scientific Research at Jouf University under grant No (DGSSR-2025-02-01462).

Author contributions

Conceptualization, KA, AA, SND; Methodology, KA, SND and MA; Software, AA, and MA; Formal Analysis, KA; MA; SND writing—original draft preparation, All Authors; writing—review and editing, All Authors; All authors have read and agreed to the published version of the manuscript.

Funding

This work was funded by the Deanship of Graduate Studies and Scientific Research at Jouf University under grant No (DGSSR-2025-02-01462).

Declarations

Competing interests

The authors declare no competing interests.

Additional information

Correspondence and requests for materials should be addressed to M.A.

Reprints and permissions information is available at www.nature.com/reprints.

Publisher's note Springer Nature remains neutral with regard to jurisdictional claims in published maps and institutional affiliations.

Open Access This article is licensed under a Creative Commons Attribution-NonCommercial-NoDerivatives 4.0 International License, which permits any non-commercial use, sharing, distribution and reproduction in any medium or format, as long as you give appropriate credit to the original author(s) and the source, provide a link to the Creative Commons licence, and indicate if you modified the licensed material. You do not have permission under this licence to share adapted material derived from this article or parts of it. The images or other third party material in this article are included in the article's Creative Commons licence, unless indicated otherwise in a credit line to the material. If material is not included in the article's Creative Commons licence and your intended use is not permitted by statutory regulation or exceeds the permitted use, you will need to obtain permission directly from the copyright holder. To view a copy of this licence, visit http://creativecommons.org/licenses/by-nc-nd/4.0/.

© The Author(s) 2025